Microstructural Analysis of the As-Welded Heat-Affected Zone of a Grade 91 Steel Heavy Section Weldment

A wide ICHAZ and delta-ferrite were observed in the HAZ

BY Y. WANG, R. KANNAN, L. ZHANG, AND L. LI

ABSTRACT

A 5-in. (127-mm) ASTM A182F91 Grade 91 steel heavy section was gas tungsten arc and flux cored arc welded. The nonequilibrium substructure of the as-welded heat-affected zone (HAZ) was characterized in multiscales. The HAZ included a narrow coarse-grained HAZ (CGHAZ) and a wide intercritical HAZ (ICHAZ). The as-welded ICHAZ exhibited the largest structural inhomogeneity with the finest grain structure, the largest fraction of the high-angle grain boundaries, and the highest local strains. Delta (δ) ferrite grains originating from the base metal were found undissolved in the HAZ. The thermodynamic simulation and composition analyses seem to suggest formation of δ-ferrite grains in the base metal were due to microsegregation of Cr, Mo, V, and Nb. These ferrite-stabilizing elements in the retained δ-ferrite grains in the HAZ had a lower concentration than that in the δ-ferrite grains of the base metal. The rejected elements may have promoted the precipitation of carbides along the interface between the δ-ferrite grains and tempered martensite.

KEYWORDS

- Grade 91 Steel • Heat-Affected Zone • Microstructure • Phase Transformation
- Heavy Section Weldment • Delta Ferrite

Introduction

ASTM A182F91 Grade 91 steel, also known as the modified 9Cr-1Mo ferritic-martensitic steel, is one of the most popular Cr-Mo creep-resistant steels used in energy industries (Refs. 1–3). The development of modern ultra-supercritical (USC) power plants requires higher operating temperatures (> 650°C) and pressures (> 30 MPa) (Refs. 2, 3). Recently, the application of Grade 91 steel, heavy section, has been considered to meet this requirement. Grade 91 steel, heavy section, has also been considered as a candidate material for nuclear power plants in replacement of lower-grade pressure vessel steels (Refs. 4–6). Fusion welding processes, such as gas tungsten arc welding (GTAW), flux cored arc welding (FCAW), and submerged arc welding (SAW), are often used to join such heavy sections during fabrication (Refs. 1, 3, 7).

Formation of the heat-affected zone (HAZ) in the weldment is unavoidable after fusion welding. It has been recognized that the HAZ microstructure governs the mechanical properties, especially the high-temperature creep behavior of welded joints (Refs. 8, 9). While most studies have focused on thinner-section Grade 91 weldments, structural evolution in the HAZ of heavy-section weldments has not been well understood. One common issue related to Grade 91 steel is short-term creep cracking, especially the infamous Type IV cracking in the fine-grained heat-affected zone (FGHAZ) or intercritical heat-affected zone (ICHAZ) (Refs. 8–10). Creep cavities in Type IV cracking preferentially nucleated close to the coarsened precipitates along the grain boundaries in the FGHAZ/ICHAZ

(Refs. 8, 9). There are numerous studies on the structure of the HAZ after post-weld heat treatment (PWHT) and high-temperature creep tests in Grade 91 pipe steel (P91) weldments (Refs. 7, 11–13). All reported results point out that the FGHAZ/ICHAZ with higher grain growth and precipitate coarsening rates has the largest creep strength reduction during PWHT and creep tests. Due to combined effects from the various PWHT parameters (temperatures and holding times) and different creep testing conditions (applied temperatures and stresses), it is difficult to identify the critical structure factor responsible for cracking issues in the HAZ.

Recently, the initial HAZ structures in the as-welded condition have been recognized to serve as the starting microstructure for the subsequent structural evolutions during PWHT and creep conditions (Ref. 13). Careful characterization of the HAZ structures with the advanced microscopic solutions provides insights to the heterogeneous features in the HAZ. To the authors' knowledge, study on the as-welded HAZ of Grade 91 heavy-section weldments has rarely been reported.

In addition to the common creep issues in the Grade 91 pipe steel weldments, the possible presence of δ-ferrite in the Grade 91 heavy-section base metal brings more complexities to welding. The δ-ferrite phase is commonly observed in the thick Grade 91 steel plates, especially the cast components (Ref. 14). The existence of the δ-ferrite is reported to decrease the toughness, ductility, and creep strength of Grade 91 steel plates (Refs.
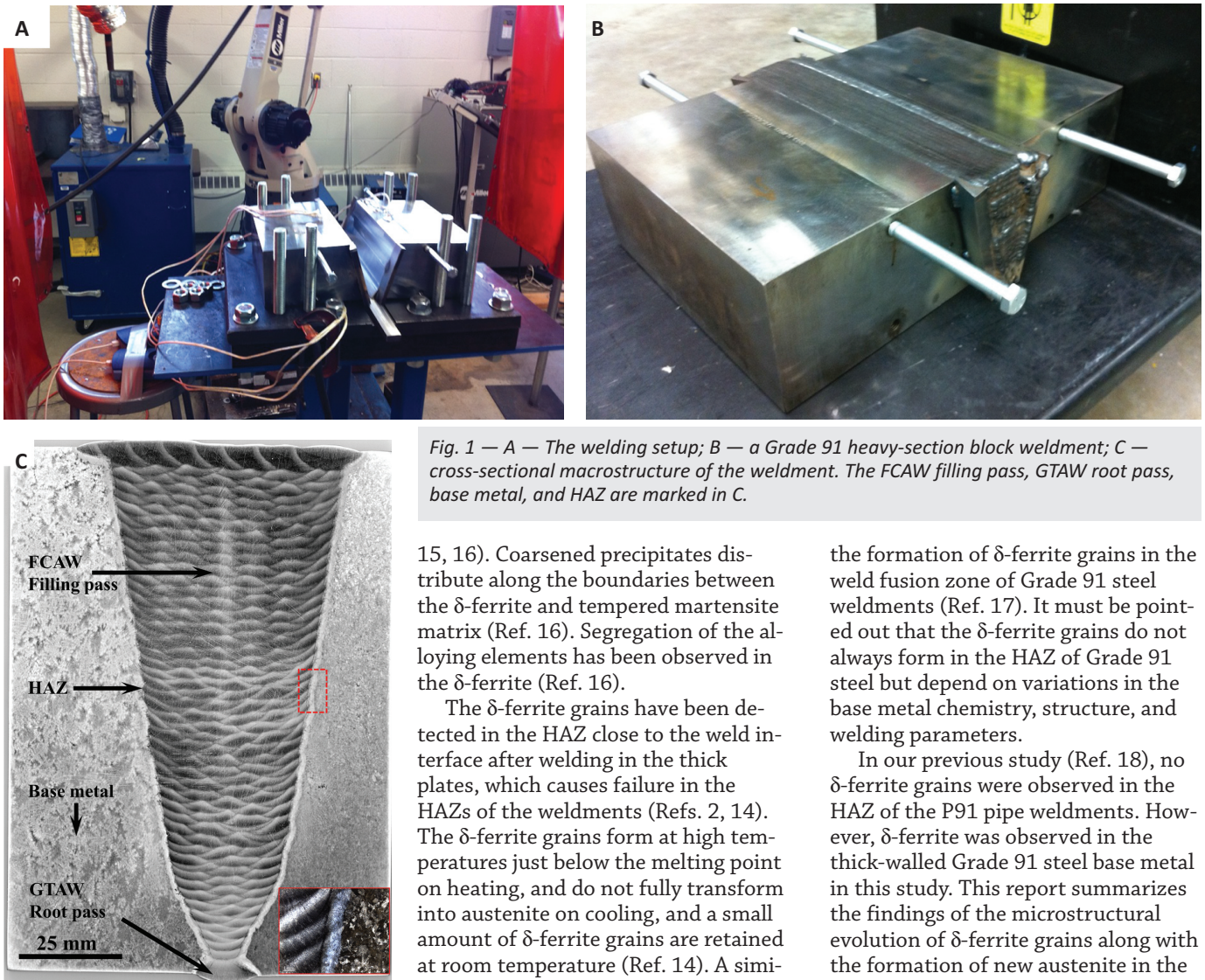
Fig. 1 — A — The welding setup; B — a Grade 91 heavy-section block weldment; C — cross-sectional macrostructure of the weldment. The FCAW filling pass, GTAW root pass, base metal, and HAZ are marked in C.

15, 16). Coarsened precipitates distribute along the boundaries between the δ-ferrite and tempered martensite matrix (Ref. 16). Segregation of the alloying elements has been observed in the δ-ferrite (Ref. 16).

The δ-ferrite grains have been detected in the HAZ close to the weld interface after welding in the thick plates, which causes failure in the HAZs of the weldments (Refs. 2, 14). The δ-ferrite grains form at high temperatures just below the melting point on heating, and do not fully transform into austenite on cooling, and a small amount of δ-ferrite grains are retained at room temperature (Ref. 14). A similar mechanism is believed to apply to the formation of δ-ferrite grains in the weld fusion zone of Grade 91 steel weldments (Ref. 17). It must be pointed out that the δ-ferrite grains do not always form in the HAZ of Grade 91 steel but depend on variations in the base metal chemistry, structure, and welding parameters.

In our previous study (Ref. 18), no δ-ferrite grains were observed in the HAZ of the P91 pipe weldments. However, δ-ferrite was observed in the thick-walled Grade 91 steel base metal in this study. This report summarizes the findings of the microstructural evolution of δ-ferrite grains along with the formation of new austenite in the HAZ of heavy-section Grade 91 steel.

Table 1 — Chemical Composition of Grade 91 Steel Heavy Section and Filler Metals (wt-%, Fe-Bal.)

| Materials	C	Cr	Mo	Mn	Si	Ni	Al	V	Nb	S	P	N
AWS A.5.28 ER90S-B9	0.07–0.13	8.0–9.5	0.80–1.10	1.25[a]	0.15–0.30	1.0[a]	0.04	0.15–0.25	0.02–0.10	0.010	0.010	0.03–0.07
ER90S-B9 GTAW (Measured)	0.097	8.830	0.928	0.560	0.250	0.307	0.002	0.197	0.064	0.004	0.006	0.030
AWS A5.29 E9XT1-B9	0.08–0.13	8.0–10.5	0.85–1.20	1.2[b]	0.50	0.80[b]	0.04	0.15–0.30	0.02–0.10	0.015	0.020	0.02–0.07
E91T1-B9 FCAW (Measured)	0.100	8.830	0.880	0.790	0.280	0.550	0.001	0.200	0.030	0.008	0.020	0.050
ASTM A182 F91	0.08–0.12	8.0–9.5	0.85–1.05	0.30–0.60	0.20–0.50	0.40	0.02	0.18–0.25	0.06–0.10	0.010	0.020	0.03–0.07
Grade 91 Base Metal (Measured)	0.086	8.890	0.870	0.390	0.330	0.300	0.003	0.220	0.096	0.001	0.020	0.034

a,b Mn + Ni = 1.5% maximum.
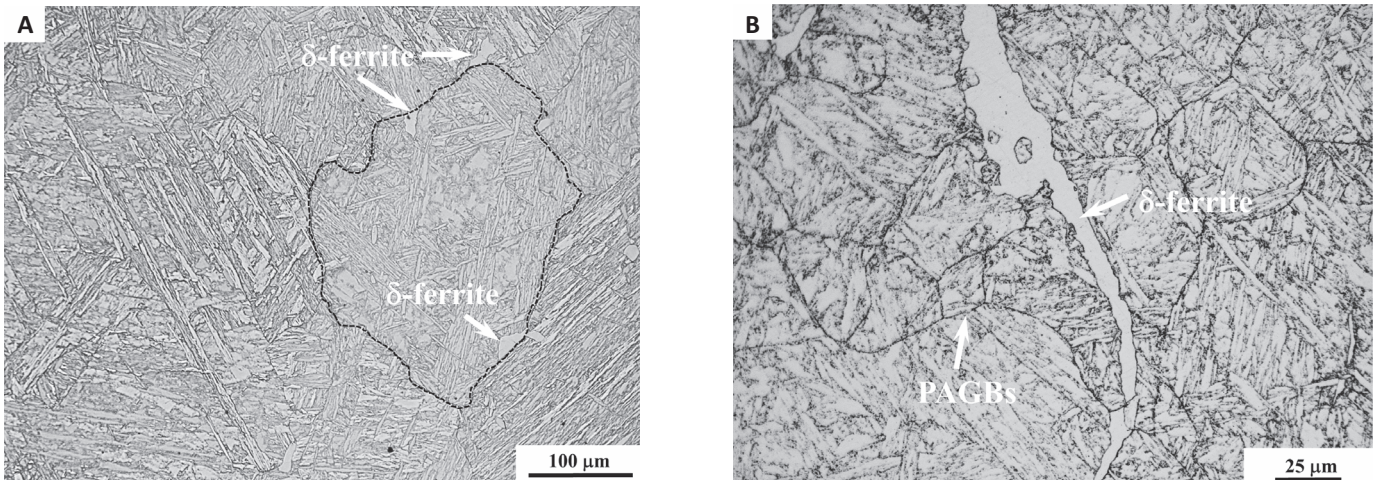
Fig. 2 — Optical microstructure of the as-received Grade 91 heavy-section block: A — Tempered martensite matrix within the coarse prior austenite grains. A prior austenite grain is highlighted by the black dash line. B — the δ-ferrite distributes along the prior austenite grain boundaries.

Materials and Methods

An ASTM A182F91 Grade 91 steel heavy-section block, used as the base metal, had a dimension of 127 mm (5 in.) thickness × 228.6 mm (9 in.) width × 304.8 mm (12 in.) length. It had been normalized at 1050°C for 3.5 h and tempered at 780°C for 3.5 h following forging. The welding setup is shown in Fig. 1A. An example of the heavy-section block weldment is shown in Fig. 1B.

Gas tungsten arc welding (GTAW) and flux cored arc welding (FCAW) were used to deposit the root and fill passes, respectively. The weld joint configuration was a compound-bevel single-groove joint design with a 60-deg included angle, 7/8 high at the bottom of the joint, and a 30-deg included angle maintained through the rest of the joint. ASTM/AWS specifications (ASTM A182 (Ref. 19), AWS A5.28 (Ref. 20), and AWS A5.29 (Ref. 21)) and measured compositions of the Grade 91 heavy-section block, GTAW filler metal ER90S-B9 (1.2 mm diameter), and FCAW filler metal E91T1-B9 (1.2 mm diameter) are shown in Table 1.

The welding parameters used in this work were the same as the 25.4-mm- (1-in.-) thick P91 pipe weldments in our previous work (Ref. 18). The GTAW parameters used for the root pass were 300 A DC and 1.27 m/min wire feed speed. Deposition of the FCAW fill passes was robotic. FCAW parameters for the fill passes were 1.0

kJ/mm heat input, 0.292 m/min linear travel speed, 27 V arc voltage, and 7.62 m/min wire feed speed. The shielding gases used for GTAW and FCAW were pure argon and mixed 75/25 argon/CO_2, respectively. The multiple temper beads were designed to improve toughness of the fusion zone. A preheat temperature of 150°C and an interpass temperature of 300°C were selected to avoid common cracking issues, especially hydrogen-induced cracking. A 4-h postweld bake was conducted at 400°C.

A cross-sectional HAZ specimen was extracted from the middle thickness of the as-welded weldment, shown in Fig. 1C. An as-received base metal specimen was also prepared for comparison. Vickers hardness across the cross section of the polished HAZ specimen was measured with a 0.5-kg force, a dwell time of 10 s, and an indentation spacing of 150 μm by using a Tukon 2500 automated hardness mapper. Hardness of the δ-ferrite grains in both base metal and HAZ were averaged from the individual indentation points. For microstructure characterization, the HAZ specimens were mounted, ground, and polished by using an automatic mechanical polisher. Grit 360, 600, and 1200 SiC sandpapers were used for grinding. The 3/1-μm diamond suspensions, 0.5/0.05-μm alumina suspensions, and 0.02-μm colloidal silica suspension were used for polishing. The electron backscatter diffraction (EBSD) analyses on the HAZ were conducted

on a Zeiss Sigma Field-Emission SEM (FESEM) equipped with an Oxford AZtec system under 20-kV accelerating voltage, a 60-μm objective aperture, and step sizes of 0.3–1.0 μm.

Specimens for EBSD characterization were polished without further etching. The polished specimens for optical and FESEM microscopic analysis were etched with 10% Nital for 2–10 min. The EBSD analyses were conducted based on indexing the 8–11 characteristic Kikuchi bands of crystal orientations and phases. The HKL Crystal Structure Database and Inorganic Crystal Structure Database (ICSD) were used for EBSD data acquisition. A postprocessing (reconstructed map) of the EBSD data was conducted by using the HKL Channel 5 software package. Matrix grain orientation was interpreted by the inverse pole figure (IPF) in Z direction (transverse direction, perpendicular to the screen).

Low-angle grain boundaries (LAGBs, misorientation θ below 10 deg) and high-angle grain boundaries (HAGBs, misorientation θ ≥ 10 deg) were distinguished by the scalar misorientation between the adjacent pixels. Grain size of the grains with HAGBs was measured from the grain boundary maps with the line-intercept method. Due to the small distortion in the lattice parameter c by the low-carbon content in the base metal, the martensite matrix is treated as body-center-cubic (bcc) iron. Misorientation maps were processed to evaluate and
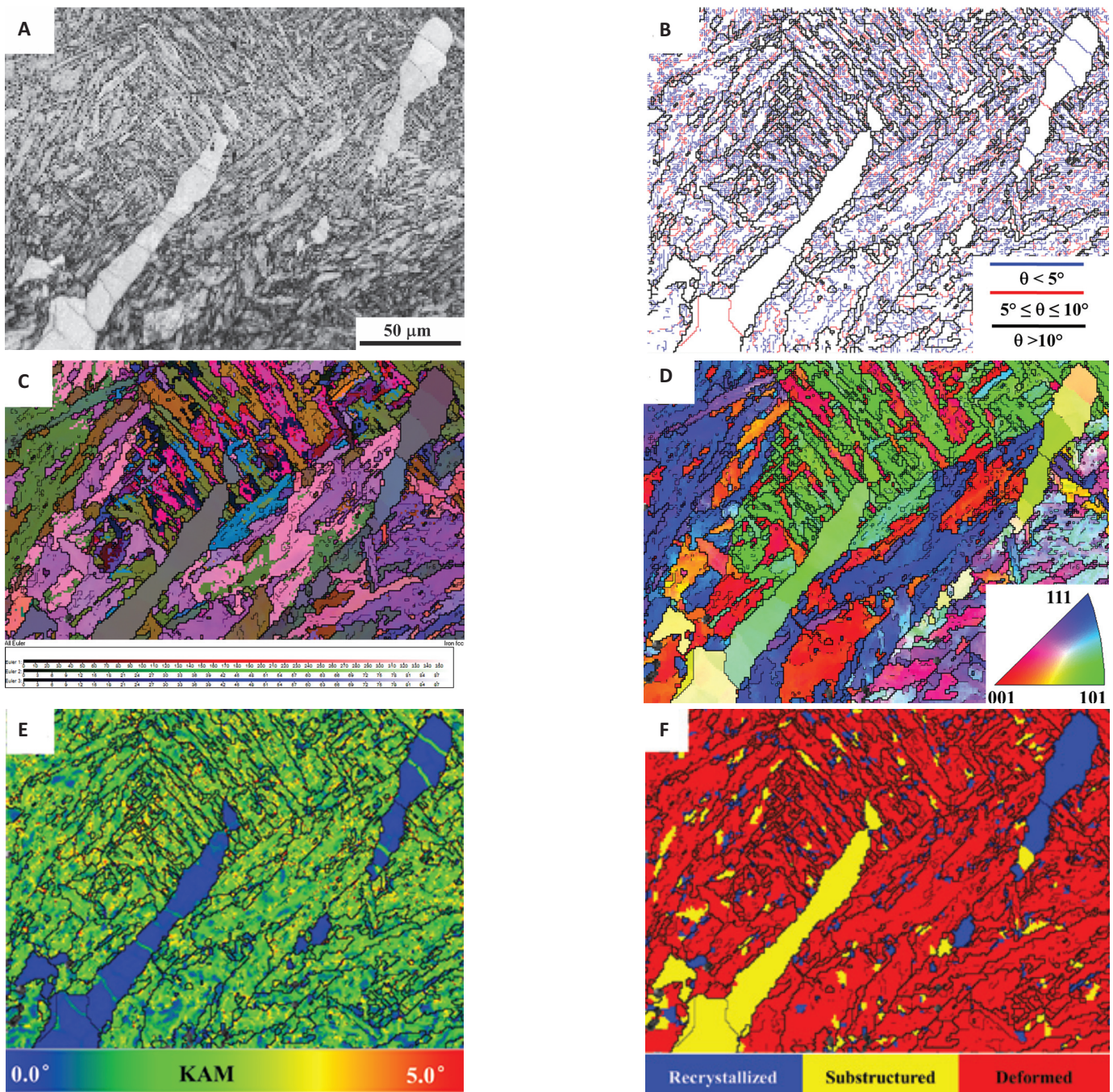
Fig. 3 — EBSD analyses of the as-received heavy-section base metal: A — Band contrast map; B — grain boundary map (black lines indicate misorientation above 10 deg, red lines indicate misorientation between 5 and 10 deg, and blue lines indicate misorientation below 5 deg); C — all Euler angle map; D — IPF in the Z direction; E — local misorientation map illustrated by KAM; F — GAM map with a threshold of 1 deg identifies three categories of grains: recrystallized, substructured, and deformed grains.

visualize the local plastic strain or deformation magnitude within grains by calculating the kernel average misorientation (KAM) between groups of pixels/kernels within the grains.

To distinguish the local strain energy difference, matrix grains were classified into recrystallized, substructured, and deformed grains by grain average misorientation (GAM) evaluation with a threshold of 1 deg (Ref. 13). The recrystallized grain had the lowest local strain energy, while the deformed grain had the highest local strain energy. The EDS mapping of the δ-ferrite grains in the HAZ was conducted under an accelerating voltage of 20 kV.

Results

Base Metal Characterization

A typical microstructure of the as-received Grade 91 heavy-section base metal, after normalizing at 1050°C for 3.5 h and tempering at 780°C for 3.5 h, is shown in Fig. 2.
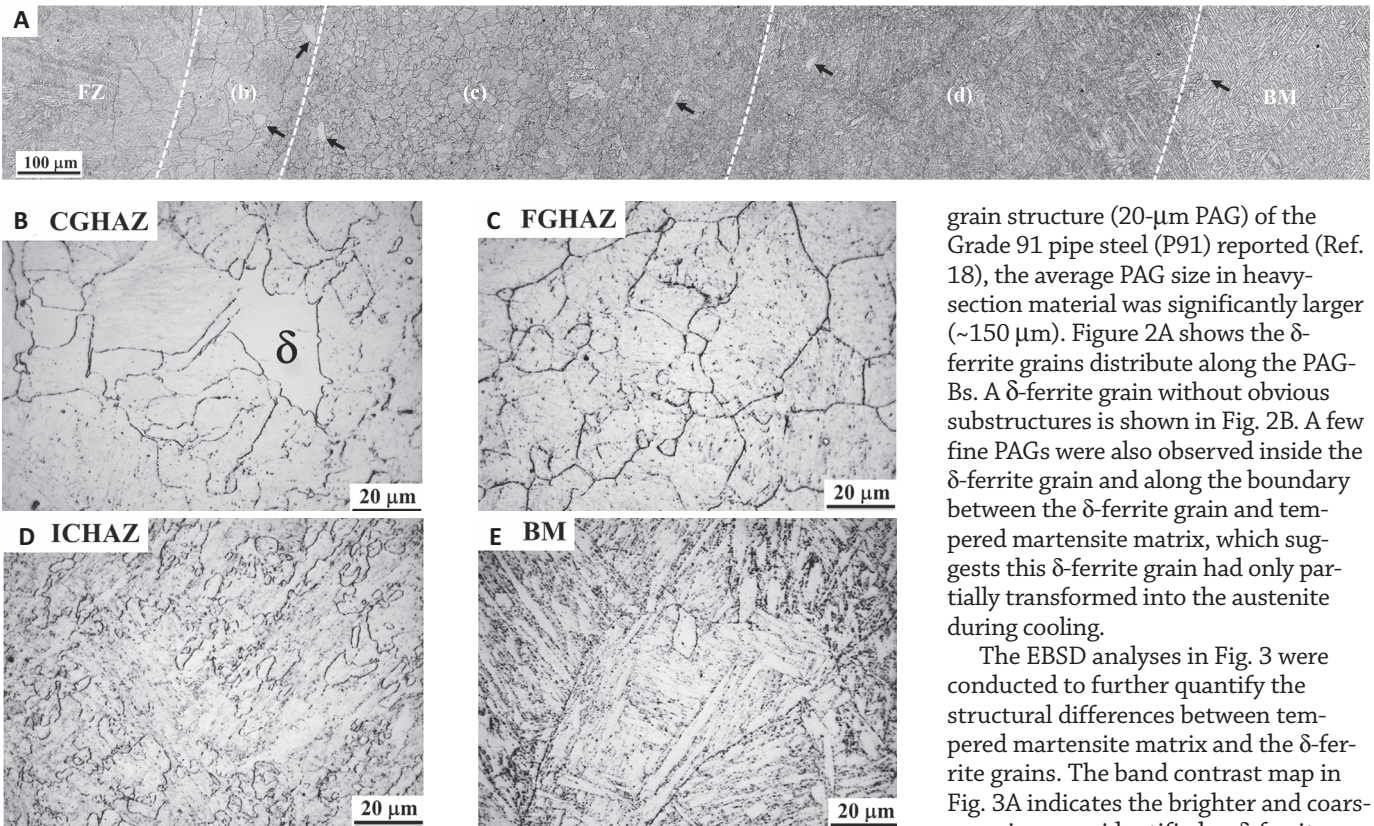
Fig. 4 — Optical microstructure of the HAZ in the as-welded condition (10% Nital etched): A — Overview of the HAZ from the FZ to the base metal; B — CGHAZ; C — FGHAZ; D — ICHAZ; E — the base metal. The δ-ferrite grains are marked by black arrows in A. The δ-ferrite grain is marked with the letter δ in B.
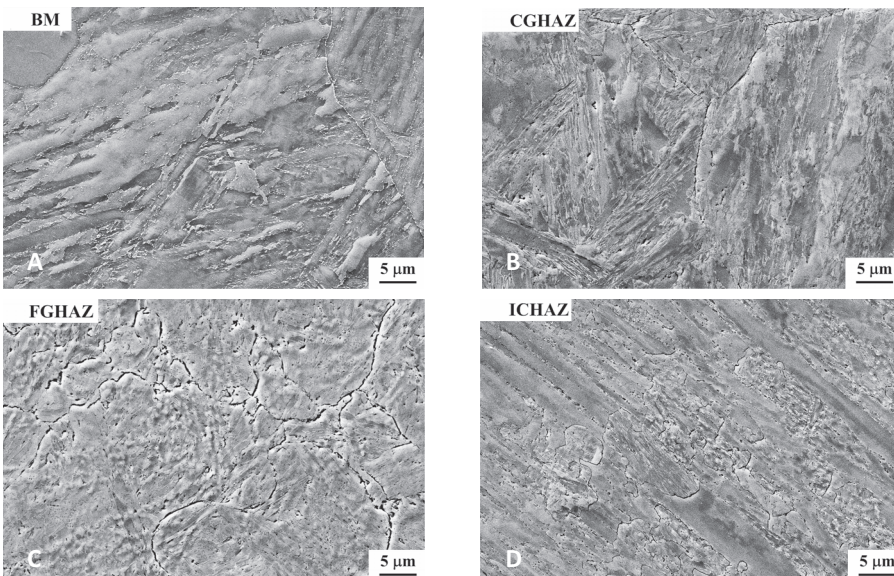

Fig. 5 — Secondary electron images of the HAZ in the as-welded condition (10% Nital etched): A — Base metal; B — CGHAZ; C — FGHAZ; D — ICHAZ.

Tempered martensitic laths were observed inside the coarse prior austenite grains (PAGs). One PAG is highlighted with the black dash lines, as shown in Fig. 2A. After tempering, precipitates (black dots in Fig. 2B) nucleated along the various boundaries, including the prior austenite grain boundaries (PAG-Bs), packet/block boundaries, and lath boundaries. Compared to the matrix grain structure (20-μm PAG) of the Grade 91 pipe steel (P91) reported (Ref. 18), the average PAG size in heavy-section material was significantly larger (~150 μm). Figure 2A shows the δ-ferrite grains distribute along the PAG-Bs. A δ-ferrite grain without obvious substructures is shown in Fig. 2B. A few fine PAGs were also observed inside the δ-ferrite grain and along the boundary between the δ-ferrite grain and tempered martensite matrix, which suggests this δ-ferrite grain had only partially transformed into the austenite during cooling.

The EBSD analyses in Fig. 3 were conducted to further quantify the structural differences between tempered martensite matrix and the δ-ferrite grains. The band contrast map in Fig. 3A indicates the brighter and coarser grains were identified as δ-ferrite grains, and the darker and finer grains were the tempered martensite matrix. The grain boundary map in Fig. 3B illustrates the boundaries between the tempered martensite matrix and δ-ferrite grains are identified as the high-angle grain boundaries (HAGBs, defined by misorientations larger than 10 deg) with black lines. It was observed there were a few sub-boundaries inside the δ-ferrite grains that were the low-angle grain boundaries (LAGBs, defined by misorientations smaller than 10 deg, blue and red lines).

The all-Euler map in Fig. 3C indicates dramatic orientation variations between different martensitic blocks; in comparison, the orientations within the δ-ferrite grains are similar in all three directions. Second, the inverse pole figure (IPF) in Fig. 3D shows those tempered martensite blocks within one PAG all having similar crystal orientations; in comparison, all δ-ferrite grains seem to show the same preferred <110> crystal orientation. The KAM map in Fig. 3E indicates the tempered martensite matrix shows high KAM values, i.e., high local misorientations or strain energy levels; in comparison, the δ-ferrite shows invariably low KAM or low-strain energy levels. The GAM map in Fig. 3F

A CGHAZ

$\theta < 5°$
$5° \leq \theta \leq 10°$
$\theta > 10°$

25 μm

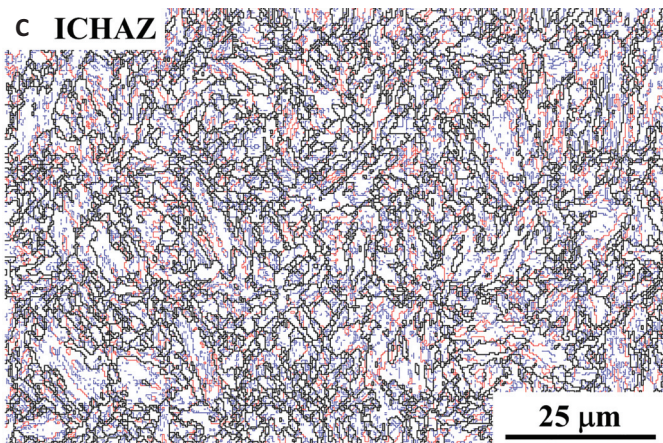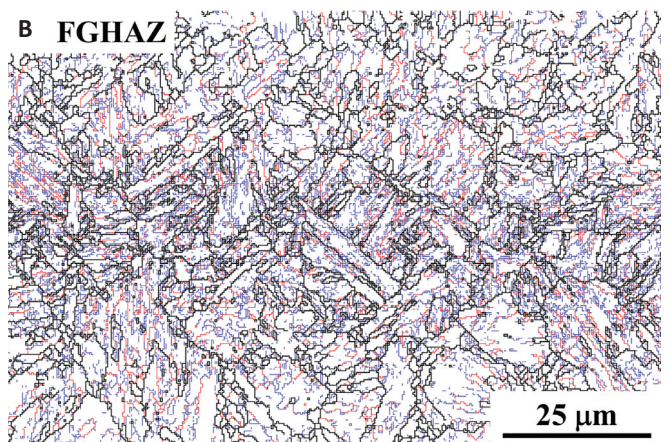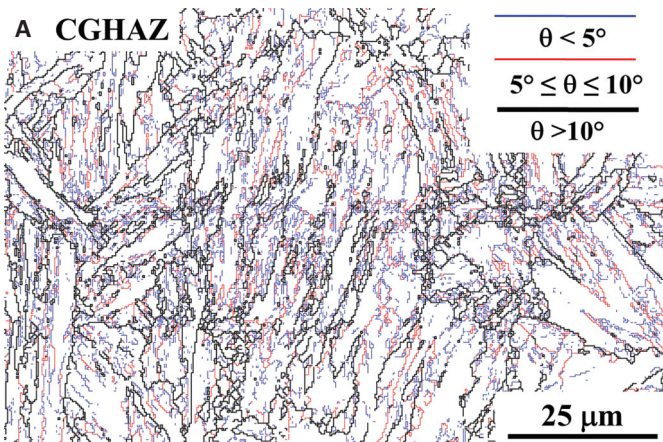**B** FGHAZ

25 μm

C ICHAZ

25 μm

Fig. 6 — EBSD grain boundary distribution maps: A — CGHAZ; B — FGHAZ; C — ICHAZ. Black lines indicate misorientation above 10 deg, red lines indicate misorientation between 5 and 10 deg, and blue lines indicate misorientation below 5 deg.

shows the majority of the martensitic matrix grains were categorized as deformed grains with the high-strain energy levels. In contrast, the δ-ferrite grains present were identified as the recrystallized or substructured (i.e., partially recrystallized) grains. In Fig. 3D and E, the martensitic blocks between the two δ-ferrite grains had larger width and lower KAM values than that of other blocks. The PAGs containing these martensitic blocks seem to suggest that there have been δ-ferrite-to-austenite transformation on cooling.

Microstructure Evolution in the HAZ Regions

Due to the rapid heating/cooling rates and peak temperature gradient in the welding process, significant structure evolutions, including austenitization, dissolution, and coarsening of the precipitates, and martensitic transformation, occur in the HAZ regions. Figure 1C shows macroetched structures of the entire weldments, including a GTAW root pass at the bottom and multiple FCAW fill passes. The width of the HAZ is narrower than 2 mm. A midthickness HAZ specimen was chosen to characterize the HAZ structures because creep cavities normally get observed in the mid-thickness HAZ after creep.

Figure 4 shows the entire structure of the HAZ and the correlated subzone structures. Based on the experienced peak temperatures and extent of tempered martensite-to-austenite transformation during the welding thermal cycles, the HAZ was further divided into coarse-grained HAZ (CGHAZ), fine-grained HAZ (FGHAZ), and inter-critical HAZ (ICHAZ). Different from the P91 pipe HAZ structures (a wide CGHAZ and FGHAZ as well as a narrow ICHAZ) reported in Ref. 18, the thickness of the CGHAZ was only a few grains wide (0.3 mm width), but the thickness (0.7 mm width) of the ICHAZ was much greater. Figure 4B shows coarse equiaxed PAGs of the CGHAZ. A δ-ferrite grain was also observed in Fig. 4B. Figure 4C shows the relatively fine equiaxed PAGs in the FGHAZ (0.7 mm width). The ICHAZ in Fig. 4D consists of fine newly formed PAGs and retained tempered martensite blocks from the base metal.

The δ-ferrite grains marked by the black arrows in Fig. 4A are observed from the high peak temperature end of the CGHAZ to the low peak temperature end of the ICHAZ. Because the morphology of the δ-ferrite grains is close to the equiaxed grains, not the skeletal or thin-string δ-ferrite grains retained from the partial δ-ferrite-austenite transformation as reported by Mayr et al. (Ref. 14), these δ-ferrite grains are believed to be retained from the base metal, rather than newly formed during the welding thermal cycles.

The SEM images in Fig. 5 show the magnified structures of each HAZ subregion and base metal. The base metal in Fig. 5A has tempered martensitic blocks with coarse dispersive precipitates along the boundaries. The CGHAZ in Fig. 5B shows a relatively new martensitic structure within coarse PAGs. The black cavities inside the PAGs are believed to be locations of the previous coarse precipitates from the base metal. A fine martensitic structure in the FGHAZ in Fig. 5C is due to martensitic transformation from the newly formed, fine PAGs. "Ghost" tracks of the previous precipitates from the base metal, shown as dots indicative of the previous PAGs in the base metal, can be observed within the newly formed PAGs.

Figure 5D shows a mixed structure of untransformed martensitic blocks from the base metal and newly transformed martensite. Coarse precipitates, identified as the Cr-rich $M_{23}C_6$ carbides (Refs. 8, 13), are observed along the martensitic blocks, and even
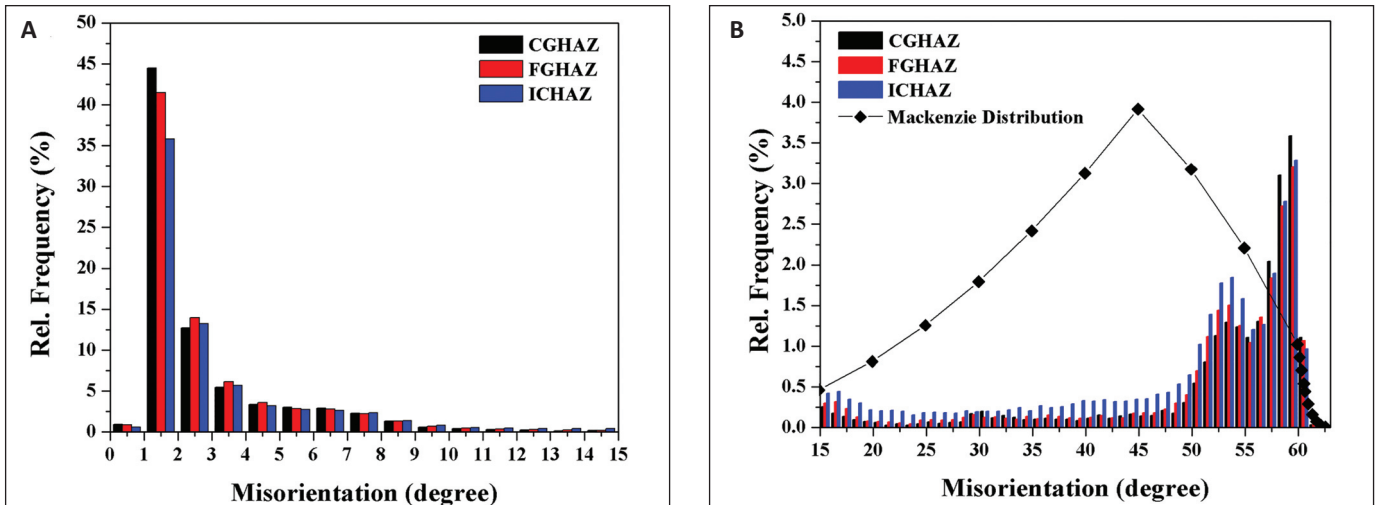
Fig. 7 — *Statistical grain boundary distribution in CGHAZ, FGHAZ, and ICHAZ: A — Low angle range; B — high angle range.*

Table 2 — EBSD GB and Grain Size Analyses on CGHAZ, FGHAZ, and ICHAZ

EBSD Measurement	CGHAZ	FGHAZ	ICHAZ
Block size by line-intercept method (μm)	2.8	2.4	1.4
Block size standard deviation (μm)	3.2	2.6	1.4
HAGB frequency (≥ 10 deg, %)	22.9	24.1	31.5
LAGB frequency (< 10 deg, %)	77.1	75.9	68.5

inside the transformed PAGs in Fig. 5D. These carbides were reported to undergo an abnormal growth during the PWHT and creep, which provide preferential nucleation sites for the creep cavities (Refs. 10, 11, 22).

Gradient welding peak temperatures in the HAZ differentiate the austenitic transformations with different PAG sizes and alloying concentrations inside the PAGs on heating, which affects the subsequent martensitic transformation on cooling by changing the morphology, size, and type of the martensite packet/block/ lath. Electron backscatter diffraction analyses were conducted on the CGHAZ, FGHAZ, and ICHAZ to visualize and quantify these structural variations.

Figure 6 shows the grain boundary distribution in the CGHAZ, FGHAZ, and ICHAZ, respectively. Figure 6A shows the thick martensitic blocks with an average size of 2.8 μm in the CGHAZ. The FGHAZ obtains a median block size of 2.4 μm — Fig. 6B. The IC-HAZ shows the finest block size of 1.4 μm — Fig. 6C.

The GB distributions in the three individual regions are plotted in Fig. 7.

Statistical analyses of the HAGB and LAGB frequencies are tabulated in Table 2. The GB distribution of the HAZ in Fig. 7B does not follow the typical Mackenzie distribution. Inversely, the CGHAZ had the lowest HAGB frequency of 22.9%; the FGHAZ had a median HAGB frequency of 24.1%; and the ICHAZ had the highest HAGB frequency of 31.5%, as shown in Table 2.

There is a complementary trend in the LAGB frequencies, as shown in Fig. 7A. The finest grain size in the ICHAZ may cause a higher susceptibility to creep strength degradation at high PWHT and creep temperatures instead of the conventional grain boundary strengthening at room temperature. The HAGBs in the ICHAZ were boundaries with higher energy and mobility; therefore, ICHAZ has a higher potential to undergo the recovery/recrystallization process, thereby lowering its creep strength.

Besides the above grain boundary distribution variations, the crystal orientations of the tempered martensitic matrix had significantly changed as well. Figure 8 represents the all-Euler

maps and IPFs of the three HAZ sub-regions, respectively. Different colors in those figures indicate various orientations. In summary, the figures (Fig. 8A and D) of CGHAZ have fewer colors, which means there were limited orientation variations within the CGHAZ. The FGHAZ (Fig. 8B and E) shows more colors, especially for these fine equiaxed grains. Due to fine PAGs formed at lower peak temperatures, the ICHAZ displays the largest orientation variations, as shown in Fig. 8C and F.

It is reported that martensitic laths in low-carbon steels normally follow the Kurdjumov-Sachs (K-S) orientation relationship (Refs. 23, 24). For low-carbon martensitic steels, six major variants likely form three groups of variant pairs (Ref. 25). In the CGHAZ, high length/width martensitic blocks with similar colors/orientations were observed within coarse PAGs. The IPF in Fig. 8D indicates there were two main variant pairs (blue-red, green-yellow) between blocks within the PAGs. In the FGHAZ, the high length/width blocks with a single color/orientation were still observed, but more equiaxed grains with gradient colors exist in the FGHAZ, as shown in Fig. 8E. In the ICHAZ, the majority of the matrix grains were fine equiaxed grains or short-length blocks with single color. Those wide blocks are believed to be untransformed (i.e., not austenitized on heating) tempered martensitic blocks from the original base metal.

The nonequilibrium martensitic transformation in the CGHAZ, FGHAZ,
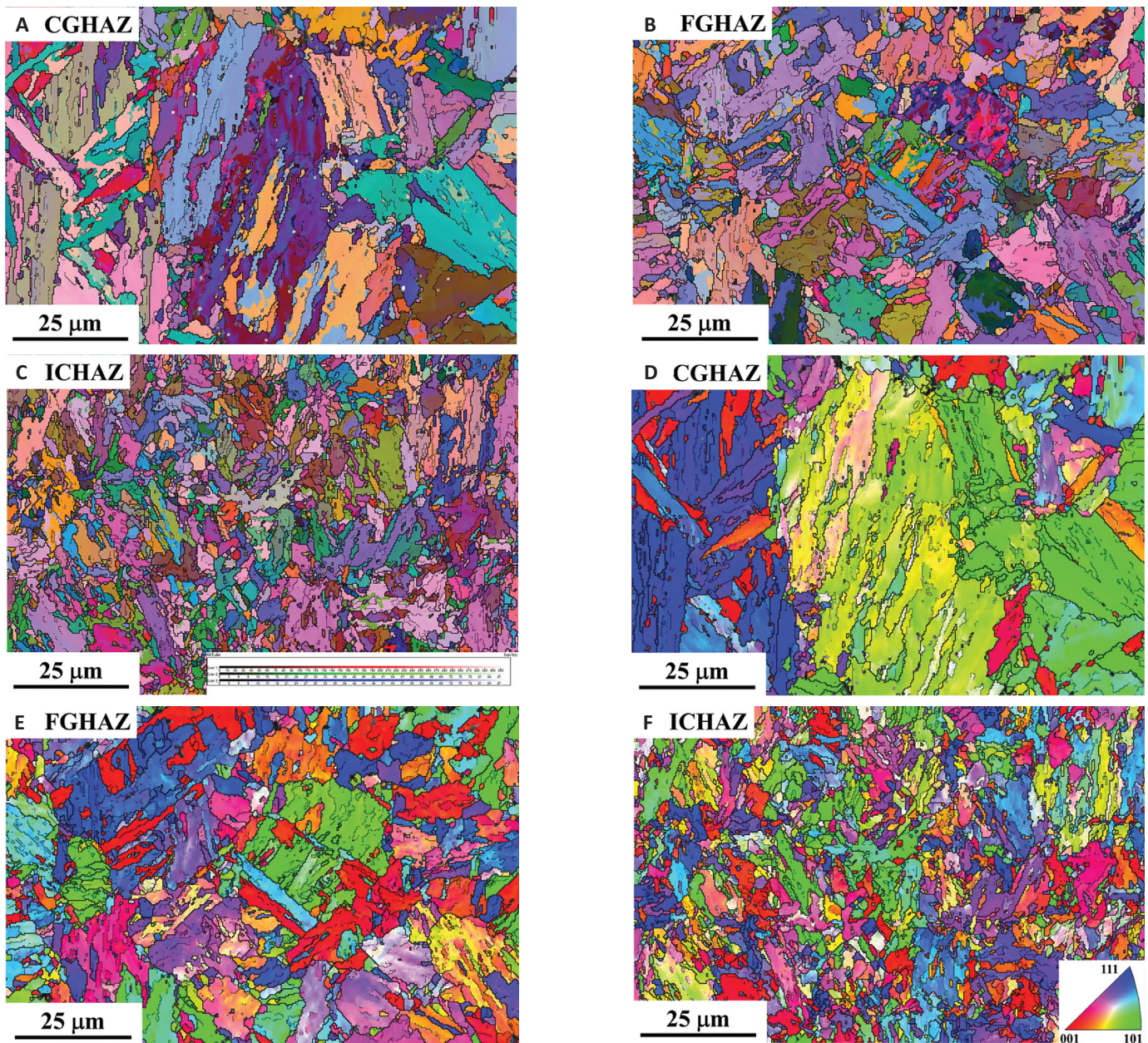
Fig. 8 — Crystal orientations illustrated by the all-Euler maps (A, B, C) and IPF in the Z direction (D, E, F): A, D — CGHAZ; B, E — FGHAZ; C, F — ICHAZ.

and ICHAZ eventually causes local strain distribution variations and different recovery/recrystallization potentials of the martensitic laths in each region. Figure 9 illustrates local strain energy variations by evaluating the KAM and GAM in the CGAHZ, FGHAZ, and IC-HAZ, respectively. The KAM and GAM reflect local misorientation inside the grains, which are sensitive to lattice distortions caused by the dislocations.

Statistical results are shown in Fig. 10 and Table 3. In summary, all three HAZs show relatively high KAM values and most of the grains are identified

Table 3 — EBSD KAM and GAM Analyses on CGHAZ, FGHAZ, and ICHAZ

EBSD Measurement	CGHAZ	FGHAZ	ICHAZ
Normalized KAM value (deg)	1.16	1.43	1.47
Deformed grain frequency (%)	75.6	87.0	84.6
Substructured grain frequency (%)	20.4	8.6	7.7
Recrystallized grain frequency (%)	4.0	4.4	7.7

as deformed grains, which have high internal strain energies. The CGHAZ shows a nonuniform KAM distribution with some high-strained grains

(green color) and some low-strained grains (blue color) in Fig. 9A. The blocks with lower KAM values were categorized as the substructured
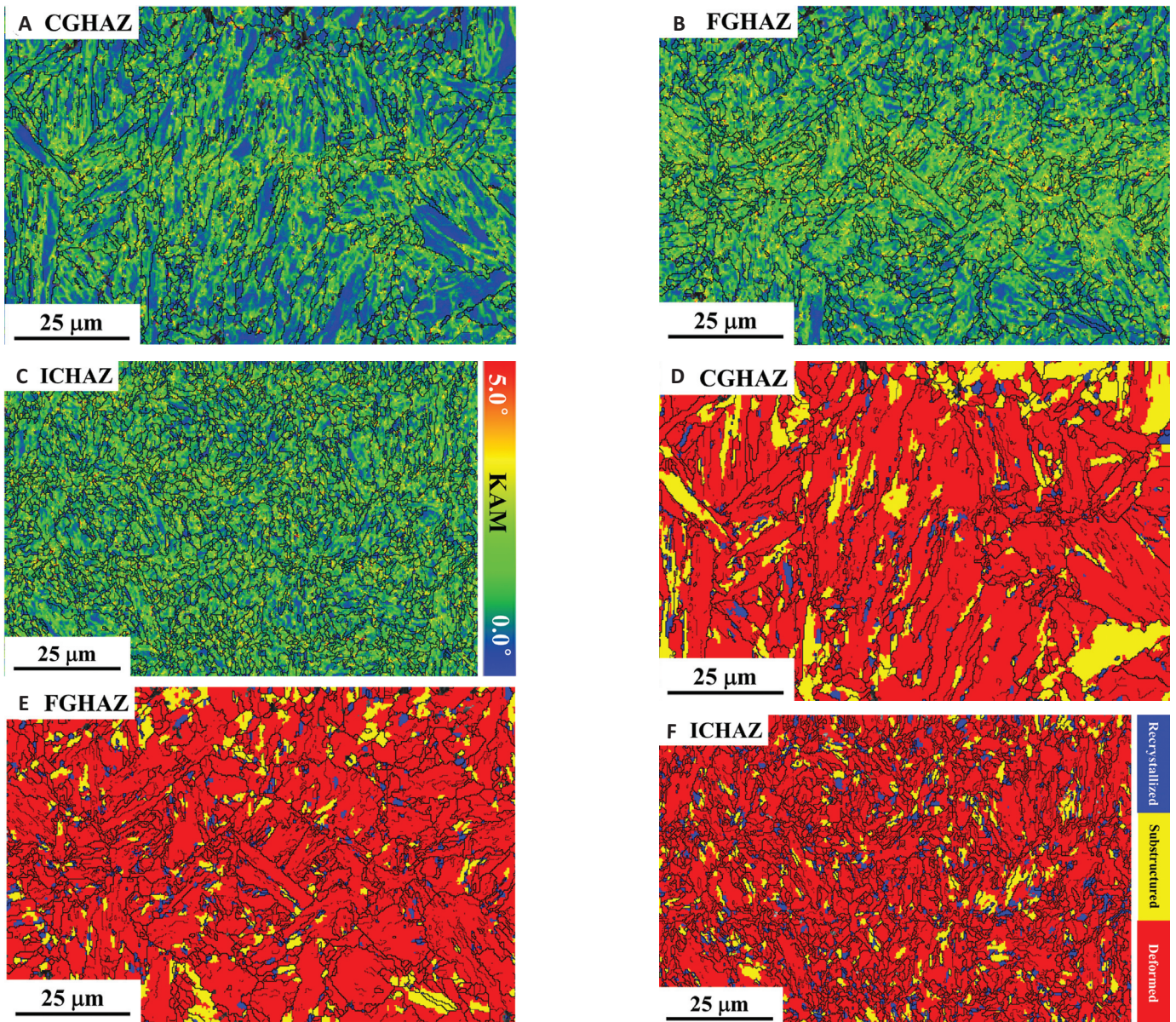
Fig. 9 — Local strain distribution illustrated by the KAM maps (A, B, C) and grain average misorientation maps (D, E, F): A, D — CGHAZ; B, E — FGHAZ; C, F — ICHAZ.

grains (20.4%, partially recrystallized) in Fig. 9D. The KAM distribution in the CGHAZ shifts toward lower values in Fig. 10A. The normalized KAM value in the CGHAZ was 1.16 deg.

The FGHAZ and ICHAZ show comparable KAM values, 1.43 and 1.47 deg, respectively. But the ICHAZ shows a more uniform KAM distribution. Both CGHAZ and FGHAZ obtain low frequencies of the recrystallized grains, 4.0 and 4.4%. The ICHAZ has a slightly higher frequency (7.7%) of recrystallized grains, which is contributed from the overtempered martensite observed in Fig. 5D. This local strain variation of

matrix grains in the CGHAZ, FGHAZ, and ICHAZ may be a significant factor for the creep strength reduction in each region during PWHT and creep. We suggest that the PWHT thermal cycle and creep testing conditions may bring a greater creep strength reduction effect on grains with a high KAM value (i.e., more dislocations), such as the deformed grains in the FGHAZ and ICHAZ.

Beside the effect of martensite matrix, particle precipitation also affects creep performance of the HAZ. It has been proven that precipitation strengthening is determined not only

by the particle size, shape, and volume fraction, but also its distribution (location). Many studies reported welding thermal cycles can cause dissolution of the precipitates in the HAZ, especially $M_{23}C_6$ carbides (Refs. 8, 9, 11). It is also reported that MX carbonitrides are barely affected during the welding thermal cycles (Refs. 1, 3). The kinetics of dissolution of Cr-rich $M_{23}C_6$ carbides was much faster, therefore affecting the creep strength to a much greater extent. It is widely recognized that the $M_{23}C_6$ carbides were completely dissolved in the CGHAZ, and partially dissolved in the FGHAZ and ICHAZ on
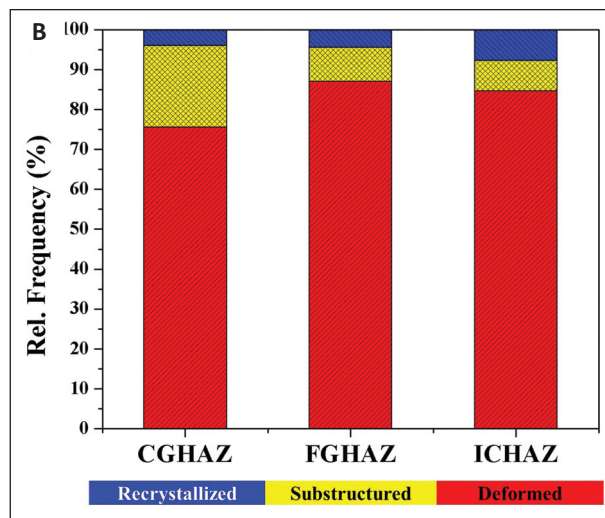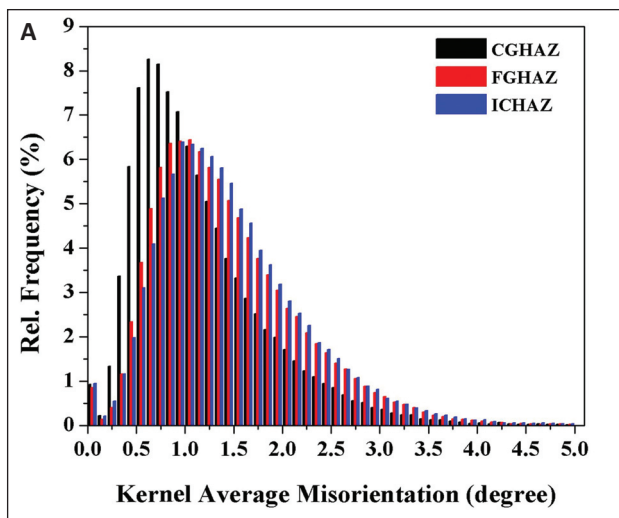
Fig. 10 — Statistical analyses of KAM and GAM distributions in the three HAZ regions: A — KAM; B — GAM.
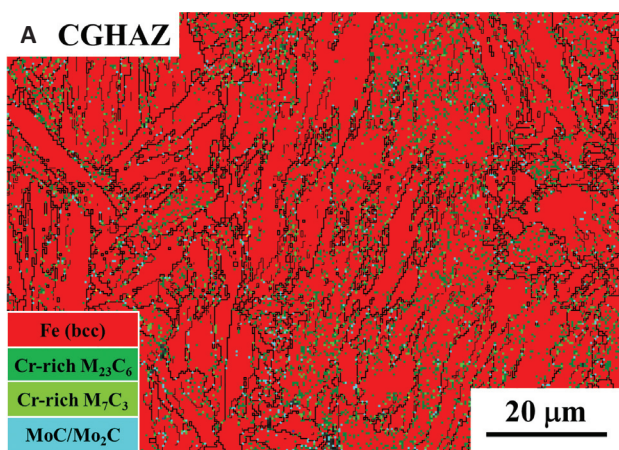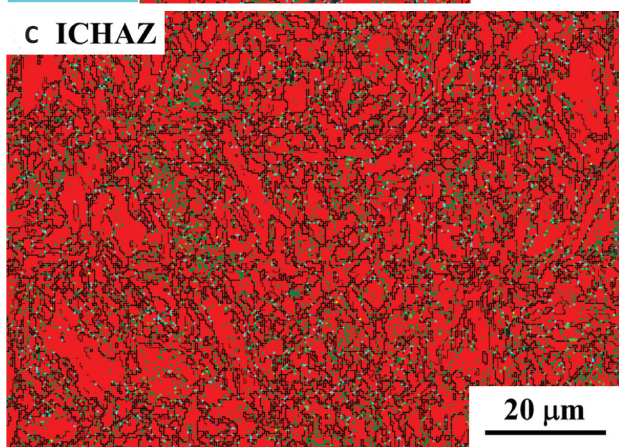

Fig. 11 — The EBSD phase distribution maps: A — CGHAZ; B — FGHAZ; C — ICHAZ.

heating (Refs. 9, 11). However, visualization of this difference is difficult. We attempted to show this difference with the help of EBSD capability.

Figure 11 represents the precipitate distributions in the CGHAZ, FGHAZ, and ICHAZ, respectively. The red background is the bcc-iron matrix. Precipitates detected by the EBSD include Cr-rich $M_{23}C_6$ carbides, Cr-rich M_7C_3 car-

bides, and Mo_2C carbides. Finer MX carbonitrides were not sufficiently detected possibly due to the limit of spatial resolution of the large step size chosen in this work. Generally, it is observed that Cr-rich $M_{23}C_6$ carbides and Cr-rich M_7C_3 carbides distribute along the PAGBs, packet/block boundaries, and some lath boundaries, which correlates with the SEM structures shown in Fig. 5A. Some Cr-rich $M_{23}C_6$ carbides inside laths were detected as well. The majority of Mo_2C carbides were observed along the boundaries.

Density variations of $M_{23}C_6$ carbides within the martensite blocks exist in all three HAZ subregions. Some

blocks were free of $M_{23}C_6$ carbides; however, some blocks had a high density of $M_{23}C_6$ carbides. This $M_{23}C_6$ carbide density variation is probably due to local alloying concentration variations from the base metal, especially the Cr concentration, which is reported in Ref. 26. This $M_{23}C_6$ carbide density difference may eventually affect the recovery/grain growth behavior and the creep deformation resistance from grain to grain.

Figure 11 shows the CGHAZ had the lowest fraction and the smallest size of Cr-rich $M_{23}C_6$ carbides. This can be explained from the fact that the CGHAZ had experienced the highest peak temperature during welding thermal cycles, and $M_{23}C_6$ carbides had significantly dissolved in the CGHAZ. The majority of these fine $M_{23}C_6$ carbides in CGHAZ were believed to have precipitated during cooling.
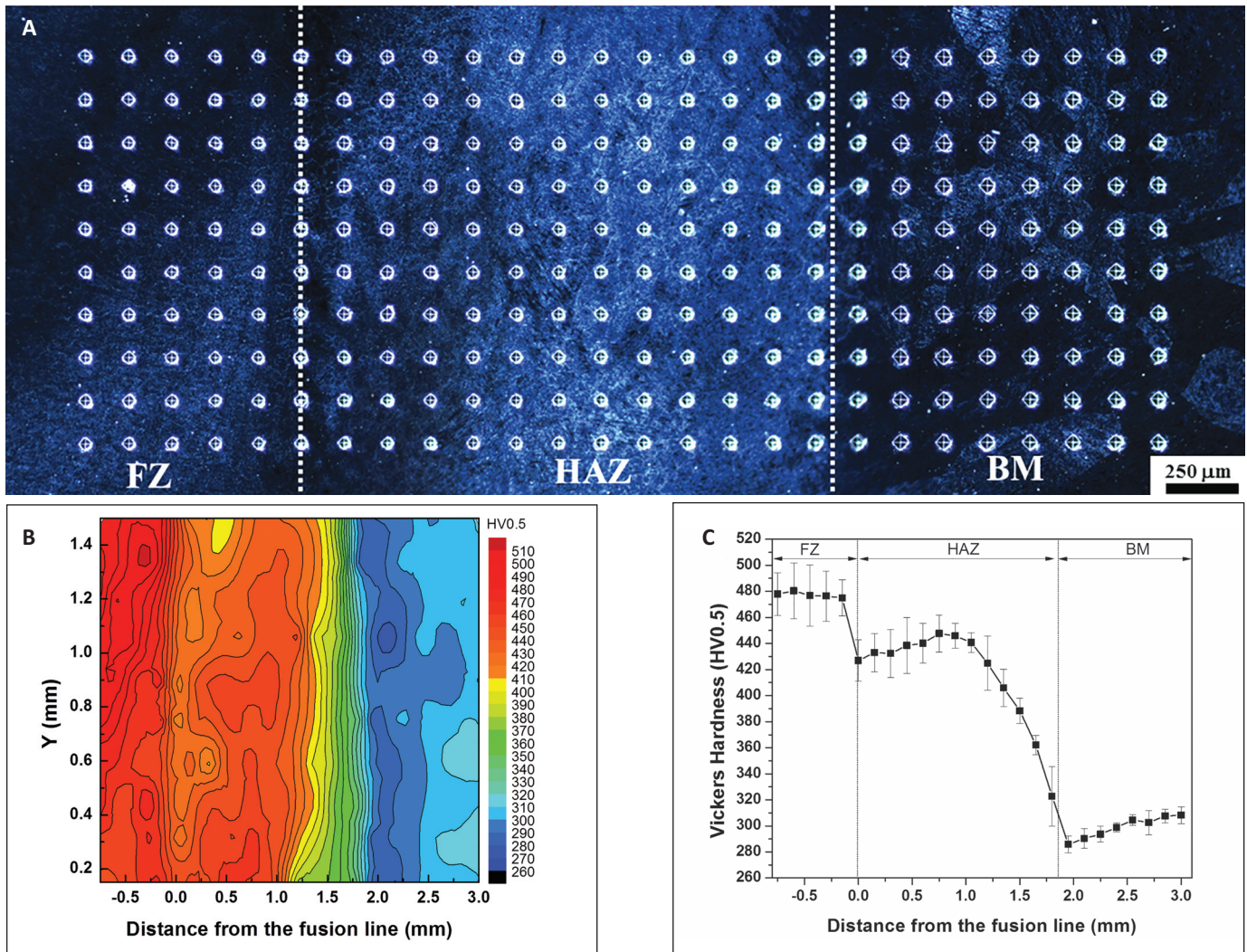
Fig. 12 — Hardness distribution in the cross-section HAZ specimen in the as-welded condition: A — Dark-field optical image of the hardness indentations; B — hardness contour map; C — average hardness distribution profile.

The ICHAZ had the highest fraction and largest size of Cr-rich $M_{23}C_6$ carbides. Figure 5D shows some $M_{23}C_6$ carbides were not completely dissolved, but retained in the newly formed PAGs. Coarsening of the $M_{23}C_6$ carbides were also observed in the ICHAZ by other researchers (Refs. 8, 9). One more observation needs to be pointed out: Figs. 11C and 5D show the retained overtempered martensite blocks (coarse grains) in the ICHAZ have nearly no $M_{23}C_6$ carbides inside. In many works, the abnormal grain growth in the ICHAZ was often observed in the Type IV cracking (Refs. 9, 11). It can be summarized that the ICHAZ not only had the largest fraction and size of $M_{23}C_6$ carbides, but also a large $M_{23}C_6$ carbide density difference between the newly trans-

formed martensite and the retained over-tempered martensite.

Microhardness Distribution

The microhardness mapping was conducted on a cross-sectional HAZ specimen, shown in Fig. 12A. Hardness contour and average hardness values are shown in Fig. 12B and C, respectively. Fusion zone (FZ) on the left side shows a high and uniform hardness value of 477 HV0.5. The base metal on the right side shows a low and uniform hardness of 304 HV0.5. In contrast, the HAZ had a nonuniform hardness distribution due to the peak temperature gradient. On both sides of the HAZ, either bordering the FZ or the base metal, the denser contour lines were seen, which means

there were larger hardness differences. The CGHAZ close to the weld interface had a relatively lower hardness than that of the CGHAZ neighboring the FGHAZ. This was probably caused by the tempering effect from the subsequent fill passes on the CGHAZ.

The KAM map in Fig. 9A shows the relatively lower local strain (and proportionally a lower hardness) in the CGHAZ, compared to that in the FGHAZ, which had the highest hardness value of 448 HV0.5. The ICHAZ close to the base metal had a low hardness of 323 HV0.5, but a large deviation (23 HV0.5). The limited martensite from the partially austenitic transformation on heating, as shown in the Fig. 5D, and the coarser and more $M_{23}C_6$ carbides, as shown in Fig. 11C, were responsible for the lower hard-
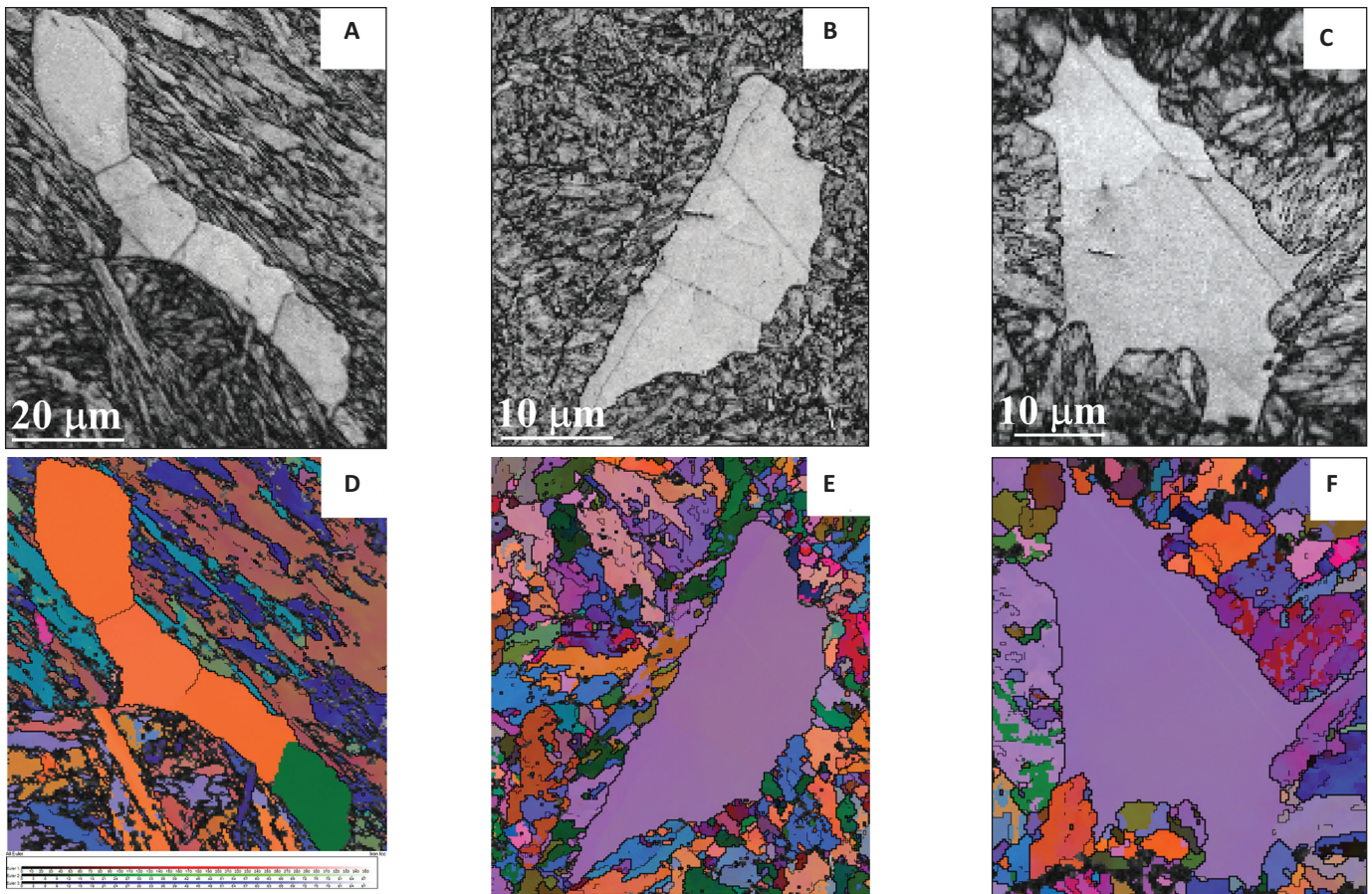
Fig. 13 — The EBSD band contrast maps (A, B, C) and all-Euler maps (D, E, F) of δ-ferrite grains in various regions: A, D — Base metal; B, E — ICHAZ; C, F — CGHAZ.

ness value. The hardness difference between the newly transformed martensite and retained overtempered martensite leads to the large hardness deviation in the ICHAZ. The softest zone with the lowest hardness of 286 HV0.5 exists in the overtempered base metal right outside the ICHAZ.

δ-Ferrite in the Base Metal and HAZ

The δ-ferrite grains were observed in the entire HAZ, including the CGHAZ adjacent to the weld interface, as shown in Fig. 4A. Figure 13 repre-

sents the band contrast and all-Euler maps of δ-ferrite grains in the base metal, IGHAZ, and CGHAZ, respectively. Based on all-Euler map, δ-ferrite grain in the base metal contains subgrains, while δ-ferrite grains in the HAZ contain no subgrains. Shape morphology of the δ-ferrite grain changes from a high length/width ratio in the base metal to a low length/width ratio in the HAZ. The large orientation variation (big color difference) between the δ-ferrite grain and martensite matrix in the base metal had decreased in the HAZ. The unique local concave curvatures of the δ-ferrite grains in

the HAZ seem to show the growth of PAGs had consumed part of the δ-ferrite grains. This reflects the diffusive mechanism of the δ-ferrite-to-austenite transformation, which was also reported by others (Refs. 14, 16).

The EDS analyses were conducted to uncover the alloying element distribution within the δ-ferrite grains. The EDS mapping in Fig. 14 shows the distribution of the ferrite-stabilizers, Cr, Mo, V, and Nb in the δ-ferrite grains in the HAZ and base metal. Higher concentrations of Cr, Mo, V, and Nb were observed in the δ-ferrite grains in both the base metal and HAZ. The distribu-

Table 4 — EDS Analyses on δ-Ferrite Grains in CGHAZ, FGHAZ, ICHAZ, and BM

Element Concentration (wt-%)	Si	V	Cr	Mn	Fe	Ni	Nb	Mo
BM-δ-ferrite	0.47	0.44	10.65	0.31	85.89	0.13	0.04	2.06
ICHAZ-δ-ferrite	0.39	0.57	10.52	0.31	86.24	0.22	0.10	1.64
FGHAZ-δ-ferrite	0.43	0.34	10.41	0.38	86.21	0.23	0.07	1.92
CGHAZ-δ-ferrite	0.45	0.37	10.34	0.44	86.57	0.18	0.10	1.53

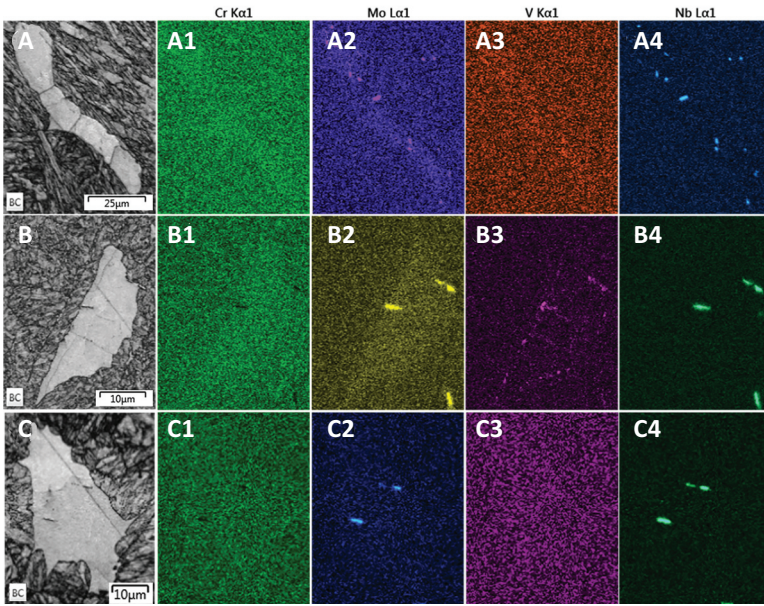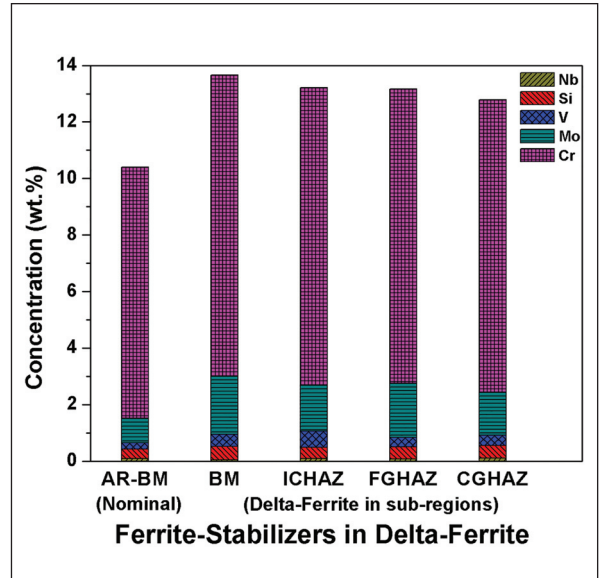Fig. 14 — EDS mapping of δ-ferrite grains in various regions: A — Base metal; B — ICHAZ; C — CGHAZ.

Fig. 15 — Accumulated concentration of ferrite stabilizers in δ-ferrite grains of the HAZ and base metal. The nominal composition of the as-received base metal is also shown.

tion of Cr was more homogeneous than Mo, V, and Nb. The particles, rich in Mo and Nb, distribute along the boundaries between δ-ferrite grains and PAGs. The Mo- and Nb-rich particles were also detected inside δ-ferrite grains in the CGHAZ, as shown in Fig. 14 C2 and C4. In Fig. 14 B3, V-rich particles were observed along the boundaries between δ-ferrite grains and PAGs. It is also noticed that concentrations (shown by the intensity) of the alloying elements, especially Cr and Mo, in δ-ferrite have decreased in the ICHAZ and CGHAZ, compared with Cr and Mo concentrations in the δ-ferrite grain of the as-received base metal.

Measured compositions of the δ-ferrite grains in both the base metal and HAZ are tabulated in Table 4. Cr concentrations inside δ-ferrite grains in the base metal were above 10 wt-%, which is higher than the nominal 8.89 wt-% Cr of this alloy. Mo concentrations inside δ-ferrite grains in the base metal are above 1.5 wt-%, which was also higher than the nominal concentration 0.87 wt-%. The Si, V, and Nb concentrations were higher than their nominal compositions as well. To show how the welding thermal cycles affect the distributions of these alloying elements, accumulated concentrations of ferrite stabilizers in the δ-ferrite grains in HAZ and base metal are shown in Fig. 15.

It can be concluded that ferrite-stabilizer elements were enriched in δ-ferrite grains in both the HAZ and base metal, but Cr and Mo concentrations in the HAZ were slightly lower than that in the base metal. Additionally, the accumulated concentration of ferrite stabilizers slightly decreased from the low peak temperature ICHAZ region to the high peak temperature CGHAZ region, which may be due to greater diffusion coefficients of those
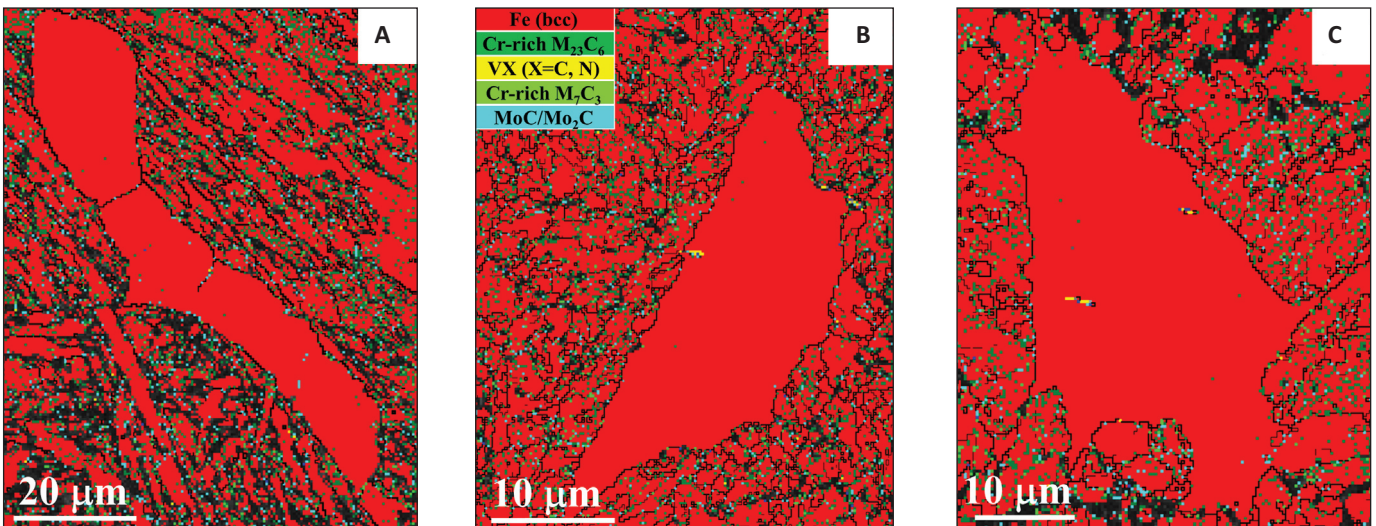

Fig. 16 — Precipitate distribution around δ-ferrite grains in various regions: A — Base metal; B — ICHAZ; C — CGHAZ.
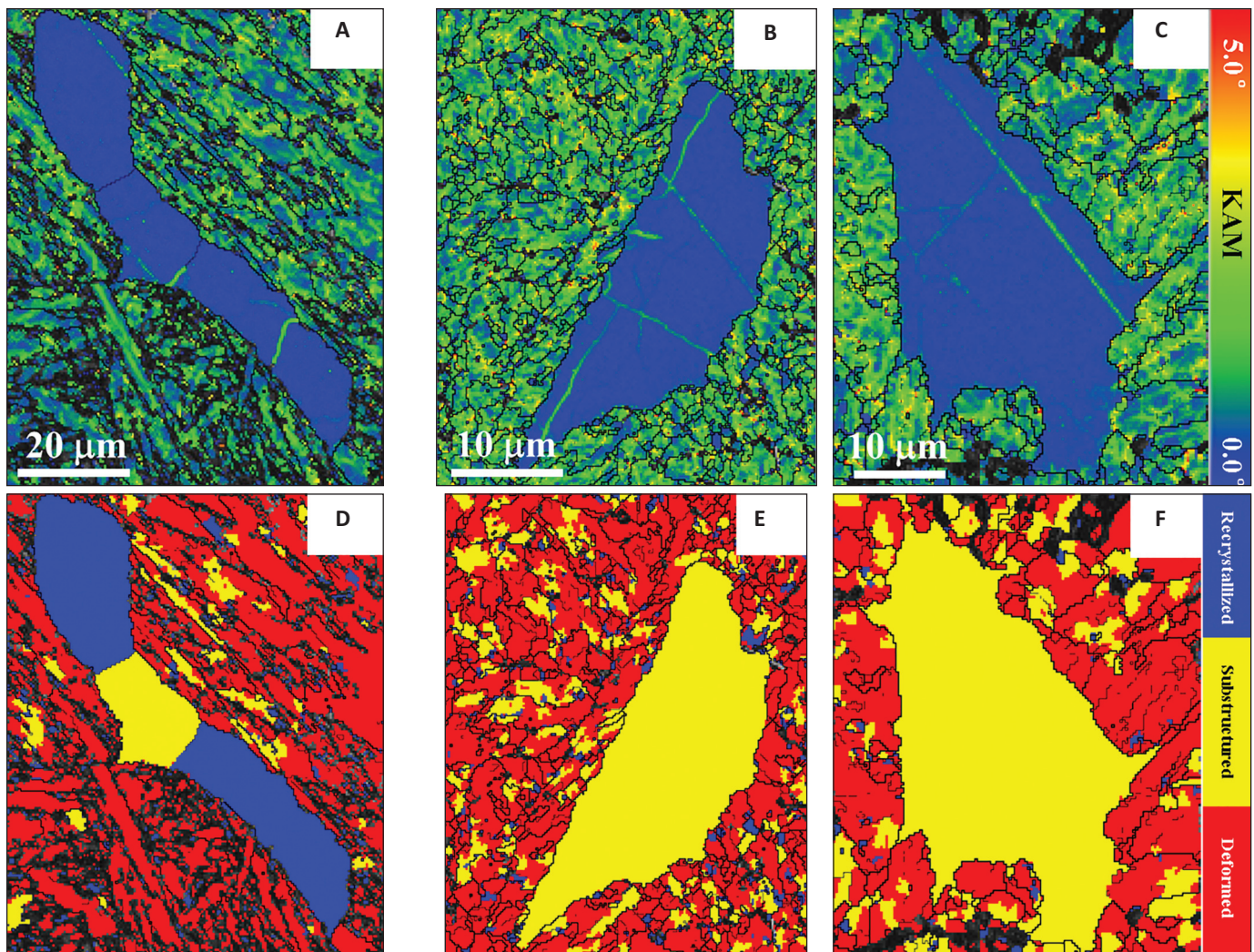
Fig. 17 — KAM (A, B, C) and GAM (D, E, F) evaluations of δ-ferrite grains in various regions: A — Base metal; B — ICHAZ; C — CGHAZ. Note: The straight line with high KAM values in C is due to a polishing scratch.

elements at higher temperatures. So, welding thermal cycles seem to have promoted the homogenization of these ferrite stabilizers by accelerating interdiffusion.

The EBSD phase maps in Fig. 16 show the precipitate distribution around the δ-ferrite grains. It can be seen that a few fine Cr-rich $M_{23}C_6$ carbides, Mo_2C carbides, and V-Nb MX carbonitrides were detected inside the δ-ferrite grains. A large amount of Cr-rich $M_{23}C_6$ carbides and Mo_2C carbides were observed along the boundaries between the δ-ferrite grains and martensitic matrix. This observation agrees with results by Kimura et al. (Ref. 15) that segregation of these carbide-forming elements in δ-ferrite grains promotes the precipitation inside and along the δ-ferrite grains. Densities of the $M_{23}C_6$ carbides in the

CGHAZ and ICHAZ had decreased, compared with that in the base metal, due to the dissolution effect from the welding heating cycles.

The EBSD KAM and GAM maps in Fig. 17 show local strain levels in the δ-ferrite grains in both the base metal and HAZ. The martensitic matrix in the HAZ shows higher KAM values than that in the base metal. Compared with the tempered martensite matrix, δ-ferrite grains in both the base metal and HAZ show relatively lower KAM values. However, the GAM maps in Fig. 17 show that part of the δ-ferrite grains in the base metal was identified as the recrystallized grains due to the previous normalization/tempering heat treatment, and δ-ferrite grains in the ICHAZ and CGHAZ were all substructured grains instead of recrystallized grains.

The local line scanning misorienta-

tion analyses in Fig. 18 show there were large misorientation changes across the subgrain boundaries of δ-ferrite grain in the base metal. Misorientation variations within δ-ferrite grains in the ICHAZ and CGHAZ, however, were larger than that in the base metal. These results seem to indicate local strain levels of δ-ferrite grains in the HAZ were higher than that of the δ-ferrite grain in the base metal. Microhardness measurements on the δ-ferrite grains had also verified this conjecture. The δ-ferrite grains in the base metal were softer than δ-ferrite grains in the HAZ. The δ-ferrite grains in the base metal had the lowest average hardness value of 240 HV0.05. The δ-ferrite grains in the ICHAZ and CGHAZ had higher average hardness values of 271 and 289 HV0.05, respectively, although the alloying element
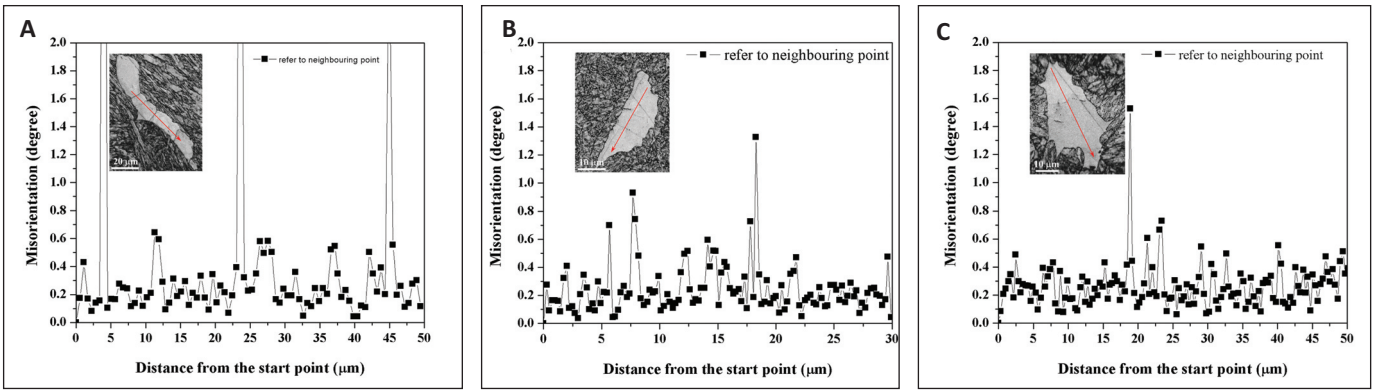
Fig. 18 — Local misorientation analysis across the δ-ferrite grains in various regions: A — Base metal; B — ICHAZ; C — CGHAZ.
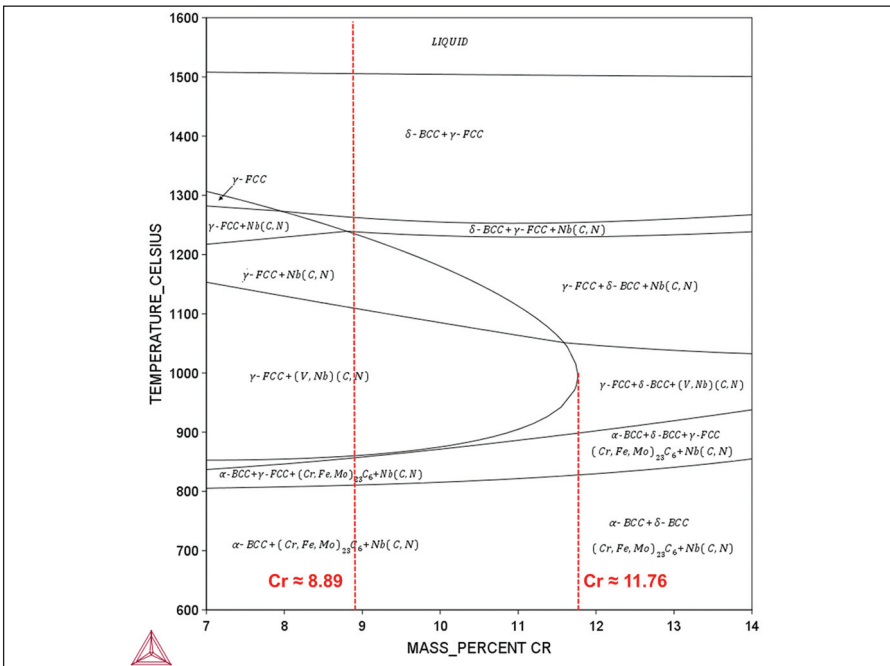

Fig. 19 — An isopleth of Grade 91 heavy-section base metal calculated by ThermoCalc.

concentrations are slightly lower.

This hardness comparison agrees with the trend shown in the KAM and GAM data. Higher local misorientation inside the δ-ferrite grain in the HAZ indicates higher straining (higher dislocation density). These increasing dislocations were believed to have generated by constraints from martensitic transformation during cooling.

Discussion

Comparing the microstructure of the 5-in. Grade 91 heavy-section HAZ in Fig. 4 with the 1-in. P91 pipe HAZ (Ref. 18), a significant difference was that the heavy-section HAZ had a narrow CG-HAZ and a wide ICHAZ, but the pipe-

HAZ had a wide CGHAZ and a narrow ICHAZ. It should be pointed out that the welding heat input for both the pipe weldment and this heavy section weldment was the same. It is our opinion that this HAZ difference was due to the steeper temperature distribution for the heavy-section weldment.

The following discussion will focus on why the identified soft zone in this as-welded thick heavy-section weldment was the overtempered base metal adjacent to the ICHAZ (Fig. 12B), not the reported FGHAZ or ICHAZ in the Type IV cracking of the pipe weldments (Refs. 3, 7). It was known that hardness in the ICHAZ was a result of two competing effects — the hardness increase due to the martensitic trans-

formation from the new PAGs, and the hardness decrease due to overtempering of martensite from the base metal. In this work, hardness in the ICHAZ gradually decreases from a higher peak temperature close to the FGHAZ to a low peak temperature close to the base metal, but without a lowest dip, as shown in Fig. 12C. This indicates the newly transformed martensite on cooling is the main contributor to hardness in the ICHAZ. For the overtempered base metal, there was only a hardness reduction effect from the welding tempering, which caused the lowest hardness (286 HV0.5).

The hardness of the normal Grade 91 base metal after normalizing and tempering was about 210–250 HV0.5, which will not be significantly reduced even after PWHT and creep. Hardness of the P91 base metal in our previous study reduced only from 230 HV1 (as-welded) to 210 HV1 (postweld heat treated at 760°C for 2 h) and 200 HV1 (crept at 650°C and 70 MPa for 649 h) (Ref. 13). A hardness of 304 HV0.5 for this heavy-section base metal was much higher than 211 HV0.5 of the P91 base metal (Ref. 18). It seems reasonable to suggest the hardness reduction in the overtempered base metal of the heavy section was larger than that of P91 pipe; therefore, the softest zone was located just outside the ICHAZ of the heavy-section weldment.

The following part is going to discuss why the δ-ferrite grains were formed in the base metal and how retained δ-ferrite grains in the HAZ may harm creep resistance of the weldment. The δ-ferrite formation traces its origin to the initial solidification during the casting process. The Cr equivalent value of 10.81 for this
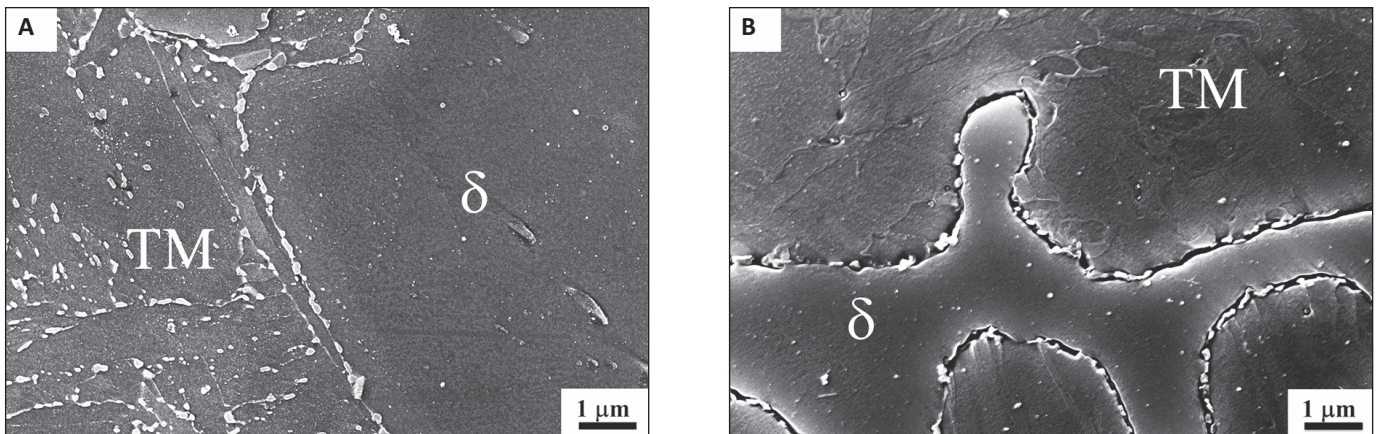
Fig. 20 — Inlens-SEM images of boundary precipitates at the interfaces between a δ-ferrite grain and martensitic matrix in the following: A — Base metal; B — CGHAZ.

heavy section steel, calculated based on the Equation 1, is higher than 10, which shows a high potential for the δ-ferrite formation (Ref. 2).

$$Cr_{eq} = Cr + 6Si + 4Mo + 1.5W + 11V + 5Nb - 40C - 30N - 4Ni - 2Mn - 2Co \, (\%) \quad (1)$$

An isopleth of the studied steel calculated by ThermoCalc, using the database TCFE6, is shown in Fig. 19. It shows that during the solidification, the δ-ferrite (δ-BCC) was the first phase nucleated from the liquid and then δ-ferrite transforms into austenite (γ-FCC) by diffusive transformation. It is our opinion that formation of the high-temperature δ-ferrite is enhanced with higher concentrations of the ferrite stabilizers, especially Cr. The left dash line shows the δ-ferrite (δ-BCC) completely transforms into austenite (γ-FCC) during a slow cooling at nominal Cr concentration of 8.89 wt-%. However, microsegregation may cause enrichment of Cr during the initial solidification of δ-ferrite (δ-BCC). Once the concentration of Cr exceeds the 11.76 wt-% (the right dashed line), a duplex region of δ-ferrite (δ-BCC) and austenite (γ-FCC) exists beyond the "austenite loop" when the temperature decreases. Those δ-ferrite (δ-BCC) grains will be retained when the temperature further cools down, which produces a mixture of ferrite (α-BCC) and δ-ferrite (δ-BCC).

The measured Cr concentration in the δ-ferrite grains in the base metal in Table 4 is lower than 11.76 wt-%, but accumulated concentration of the ferrite stabilizers in Fig. 15 exceeds 11.76 wt-%. Another factor is that the subsequent normalizing and tempering processes may have homogenized (decreased) the as-cast distribution of Cr as well. So it was likely that the δ-ferrite grain in the as-received base metal had initially formed due to microsegregation during the solidification. For δ-ferrite grains in the HAZ, Cr concentration slightly decreases, but the accumulated concentration of the ferrite stabilizers is still beyond 11.76 wt-%. This seems to support the contention that a duplex structure (α-BCC + δ-BCC) in the HAZ is thermodynamically stable after cooling.

The presence of those δ-ferrite grains in the HAZ brings potential harm to the creep strength, as reported by others (Refs. 14–16). Figure 20 compares the boundary precipitates between the δ-ferrite grain and martensitic matrix in the base metal, and the CGHAZ. A higher density of precipitates distributes along the boundaries between the δ-ferrite grain and martensitic matrix in the base metal. Precipitates along the boundaries between δ-ferrite grain and martensitic matrix in the CGHAZ were believed to be the undissolved precipitates from the base metal. The EBSD phase map in Fig. 16C shows those precipitates are the $M_{23}C_6$ and Mo_2C carbides. High alloying concentrations in δ-ferrite grains, as shown in the EDS maps in Fig. 14, may promote a preferential coarsening of these carbides during PWHT and high-temperature creep service.

Coarsened boundary carbides and δ-ferrite grains can cause local stress concentration, which provides the preferential nucleation sites for the creep cavities. To eliminate δ-ferrite grains in the base metal and improve creep resistance of the weldments, a heat treatment should be conducted. Increasing the normalizing holding time is reported to dissolve the δ-ferrite grains (Ref. 16), but the kinetics for eliminating the δ-ferrite grains still needs further investigation.

Conclusions

The 5-in.-thick-walled ASTM A182 F91 Grade 91 steel heavy sections were successfully welded with FCAW and GTAW.

The nonequilibrium microstructure of the HAZ in the as-welded condition was systematically studied. Islands of δ-ferrite along the prior austenite grain (PAG) boundaries and tempered martensite constitute the typical microstructure of the as-received heavy-section base metal. The as-welded HAZ of this heavy section was distinguished by a narrow CGHAZ, a wide FGHAZ, and a wide ICHAZ. Martensitic transformation from coarse and fine PAGs contributed to various local strain distributions in the CGHAZ and FGHAZ. The ICHAZ had the finest structure with an average martensitic block width of 1.4 μm, the largest local strain distribution with a normalized KAM value of 1.47 deg, and large frequency (84.6%) of the deformed grains with higher strain energies. This high structural inhomogeneity may lead to preferential coarsening and strength reduction of ICHAZ dur-

ing PWHT, which eventually makes it more vulnerable to creep deformation and cracking during creep.

The overtempered base metal, instead of FGHAZ or ICHAZ, had the lowest hardness value of 286 HV0.5 due to the dominant tempering effect from welding thermal cycles. Microsegregation of the ferrite stabilizing elements in the δ-ferrite grains, originated from the initial base metal, thermodynamically stabilized its presence in the HAZ after welding. Decomposition of the δ-ferrite grains in the HAZ favored precipitation of dense carbides along the boundaries with the adjacent tempered martensite matrix, which may be harmful to creep resistance of the HAZ.

A heat treatment needs to be conducted on the base metal to eliminate the δ-ferrite grains before welding.

References

1. Francis, J., Mazur, W., and Bhadeshia, H. 2006. Review Type IV cracking in ferritic power plant steels. *Materials Science and Technology* 22(12): 1387–1395.

2. Abe, F., Kern, T., and Viswanathan, R. 2008. *Creep-Resistant Steels, Series in Metals and Surface Engineering*. Cambridge, Woodhead Publishing.

3. David, S., Siefert, J., and Feng, Z. 2013. Welding and weldability of candidate ferritic alloys for future advanced ultrasupercritical fossil power plants. *Science and Technology of Welding and Joining* 18(8): 631–651.

4. Klueh, R., and Nelson, A. Ferritic/martensitic steels for next-generation reactors. 2007. *Journal of Nuclear Materials* 371(1): 37–52.

5. Swindeman, R., Santella, M., Maziasz, P., Roberts, B., and Coleman, K. 2004. Issues in replacing Cr-Mo steels and stainless steels with 9Cr-1Mo-V steel. *International Journal of Pressure Vessels and Piping* 81(6): 507–512.

6. Zhang, K., and Aktaa, J. 2016. Characterization and modeling of the ratcheting behavior of the ferritic-martensitic steel P91. *Journal of Nuclear Materials* 472(4): 227–239.

7. Silwal, B., Li, L., Deceuster, A., and Griffiths, B. 2013. Effect of postweld heat treatment on the toughness of heat-affected zone for Grade 91 steel. *Welding Journal* 92(3): 80-s to 87-s.

8. Laha, K., Chandravathi, K., Parameswaran, P., Rao, K., and Mannan, S. 2007. Characterization of microstructures across the heat-affected zone of the modified 9Cr-1Mo weld joint to understand its role in promoting Type IV cracking. *Metallurgical and Materials Transactions A* 38(1): 58–68.

9. Mayr, P., Schlacher, C., and Mitsche, S. 2011. Critical issues with creep exposed ferritic-martensitic welded joints for thermal power plants. *International Conference of the IIW*: 417–425.

10. Abson, D., and Rothwell, J. 2013. Review of Type IV cracking of weldments in 9-12%Cr creep strength enhanced ferritic steels. *International Materials Reviews* 58(8): 437–473.

11. Albert, S., Matsui, M., Watanabe, T., Hongo, H., Kubo, K., and Tabuchi M. 2003. Variation in the Type IV cracking behaviour of a high Cr steel weld with post weld heat treatment. *International Journal of Pressure Vessels and Piping* 80(6): 405–413.

12. Gao, Q., Di, X., Liu, Y., and Yan, Z. 2012. Recovery and recrystallization in modified 9Cr-1Mo steel weldments after post-weld heat treatment. *International Journal of Pressure Vessels and Piping* 93: 69–74.

13. Wang, Y., and Li, L. 2016. Microstructure evolution of fine-grained heat affected zone in Type IV failure of P91 welds. *Welding Journal* 95(1): 27-s to 36-s.

14. Mayr, P., Palmer, T., Elmer, J., Specht, E. D., and Allen, S. 2010. Formation of delta ferrite in 9 wt.% pct Cr steel investigated by in-situ X-ray diffraction using synchrotron radiation. *Metallurgical and Materials Transactions A* 41(10): 2462–2465.

15. Kimura, K., Sawada, K., Toda, Y., and Kushima, H. 2007. Creep strength assessment of high chromium ferritic creep resistant steels. *Materials Science Forum* 539: 3112–3117.

16. Kobayashi, S., Sawada, K., Hara, T., Kushima, H., and Kimura, K. 2014. The formation and dissolution of residual δ-ferrite in ASME grade 91 steel plates. *Materials Science and Engineering: A* 592: 241–248.

17. Vijayalakshmi, M., Saroja, S., Thomas Paul, V., Mythili, R., and Raghunathan, V. S. 1999. Microstructural zones in the primary solidification structure of weldment of 9Cr-1Mo steel. *Metallurgical and Materials Transactions A* 30(01): 161–174.

18. Wang, Y., Kannan, R., and Li, L. 2016. Characterization of as-welded microstructure of heat-affected zone in modified 9Cr-1Mo-V-Nb steel weldment. *Materials Characterization* 118: 225–234.

19. ASTM International. ASTM A182/A182M-16a *Standard Specification for Forged or Rolled Alloy and Stainless Steel Pipe Flanges, Forged Fittings, and Valves and Parts for High-Temperature Service*. West Conshohocken, Pa.: ASTM International, 2016. DOI: *https://doi.org/10.1520/A0182_A0182M-16A*.

20. AWS A5.28/A5.28M. 1996. *Specification for Low-Alloy Steel Electrodes and Rods for Gas Shielded Arc Welding*. Miami, Fla.: American Welding Society.

21. AWS A5.29/A5.29M. 2010. *Specification for Low Alloy Electrodes for Flux Cored Arc Welding*. 4th Ed. Miami, Fla.: American Welding Society.

22. Abe, F. 2008. Precipitate design for creep strengthening of 9% Cr tempered martensitic steel for ultra-supercritical power plants. *Science and Technology of Advanced Materials* 9(1): 013002.

23. Nishiyama, Z. 1978. *Martensitic Transformation*. Academic Press Inc.

24. Morito, S., Huang, X., Furuhara, T., Maki, T., and Hansen N. 2006. The morphology and crystallography of lath martensite in alloy steels. *Acta Materialia* 54(19): 5323–5331.

25. Morito, S., Tanaka, H., Konishi, R., Furuhara, T., and Maki, T. 2003. The morphology and crystallography of lath martensite in Fe-C alloys. *Acta Materialia* 51(6): 1789–1799.

26. Sawada, K., Hara, T., Tabuchi, M., Kimura, K., and Kubushiro, K. 2015. Microstructure characterization of heat affected zone after welding in Mod.9Cr-1Mo steel. *Materials Characterization* 101: 106–113.

YIYU WANG, RANGASAYEE KANNAN, and LEIJUN LI (leijun@ualberta.ca) *are with the University of Alberta, Edmonton, Alberta, Canada. WANG and LIANMENG ZHANG are with the Wuhan University of Technology, Wuhan, China.*